Supplementary Information

Ni-Sn intermetallics as efficient buffering matrix of Si anodes in Li-ion batteries

Tahar Azib[a,*] , Nicolas Bibent[b], Michel Latroche[a], Florent Fischer[c], Jean-Claude Jumas[b],

Josette Olivier-Fourcade[b], Christian Jordy[c], Pierre-Emmanuel Lippens[b], Fermin Cuevas[a]

[a] *Univ Paris Est Creteil, CNRS, ICMPE, 2 rue Henri Dunant, 94320 Thiais, France.*
[b] *ICGM, UMR 5253 CNRS, Université de Montpellier, Place Eugène Bataillon, 34095 Montpellier Cedex 5, France.*
[c] *SAFT Batteries. 113 Bd. Alfred Daney, 33074 Bordeaux Cedex. France.*

* Corresponding author: azib@icmpe.cnrs.fr

EPMA images and data analysis for the three intermetallic samples A, AB and B are displayed in Fig. S1. The chemical composition for the major phases is gathered in Table S1. As concerns EPMA images (obtained in BSE mode), black areas represent low electronic density regions attributed to either the epoxy resin binder or powder porosity. For sample A, major phase in grey corresponds to Ni_3Sn_2 phase, whereas small white areas are identified as minor Ni_3Sn impurity (not detected by XRD in Fig. 1). For sample AB, two grey phases of different tonality were observed and identified as Ni_3Sn_2 and Ni_3Sn_4. For sample B, only the Ni_3Sn_4 phase was detected.

Table S1. Composition of major phases in A, AB and B samples as determined by EPMA. Standard deviations referred to the last digit are given in parenthesis.

Sample	Phase	# Data analysis	Composition
A	Ni_3Sn_2	30	$Ni_{3.08(3)}Sn_{2.00(3)}$
AB	Ni_3Sn_2	29	$Ni_{2.59(1)}Sn_{2.00(1)}$
	Ni_3Sn_4	17	$Ni_{3.69(2)}Sn_{4.00(1)}$
B	Ni_3Sn_4	66	$Ni_{3.55(1)}Sn_{4.00(1)}$
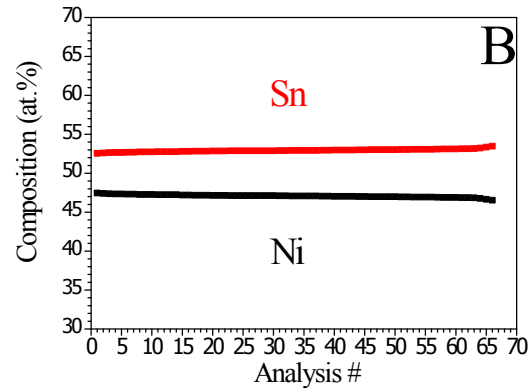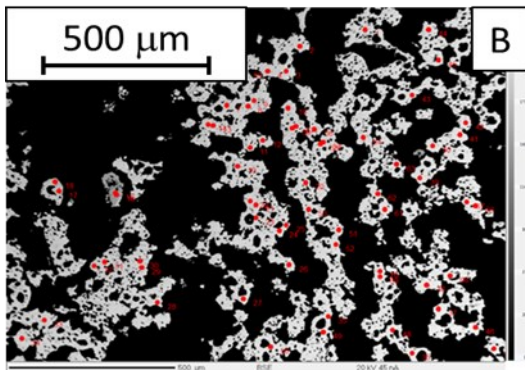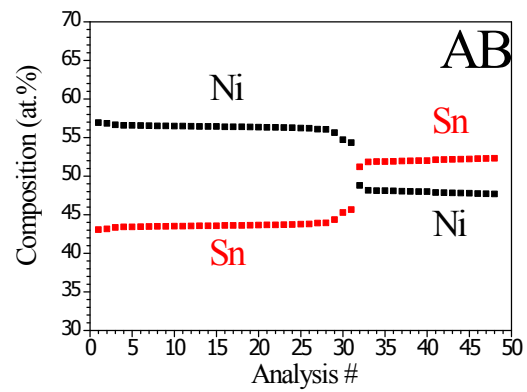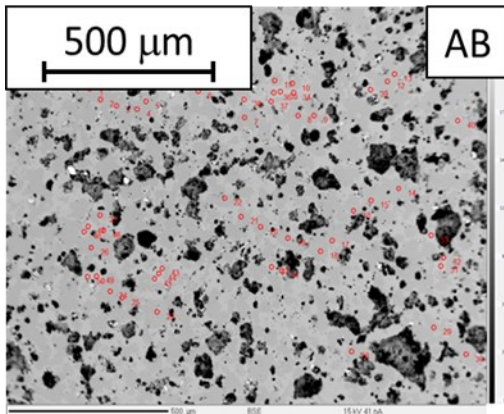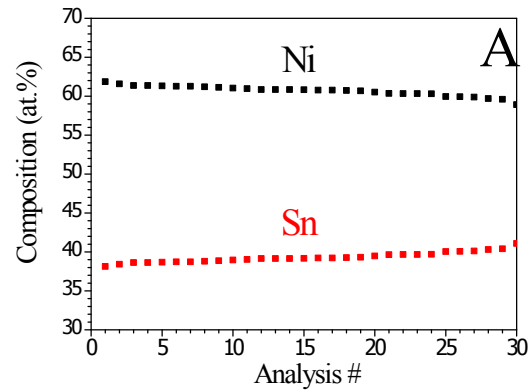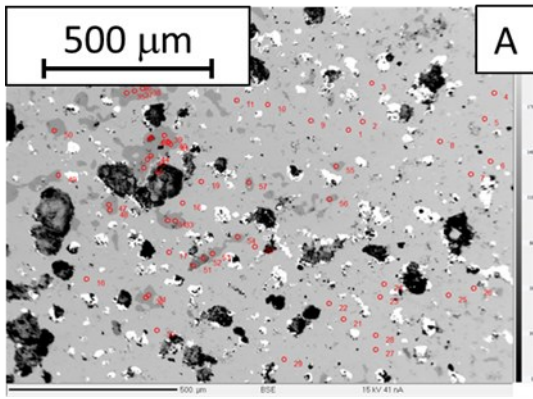
Fig. S1. EPMA chemical analysis of Ni-Sn intermetallics. Samples A, AB and B are displayed in top, middle and bottom graphs. Left: EPMA images in BSE mode, Right: chemical analysis (sorted by increasing Sn-content) at random sample locations (shown as red data points in left images)

The graphical output of the Rietveld analysis of XRD patterns of the three intermetallic samples A, B and AB are shown in Fig. S2. All diffraction peaks can be indexed with single phase Ni_3Sn_2 (sample A), Ni_3Sn_4 (sample B) or combination of both (sample AB).
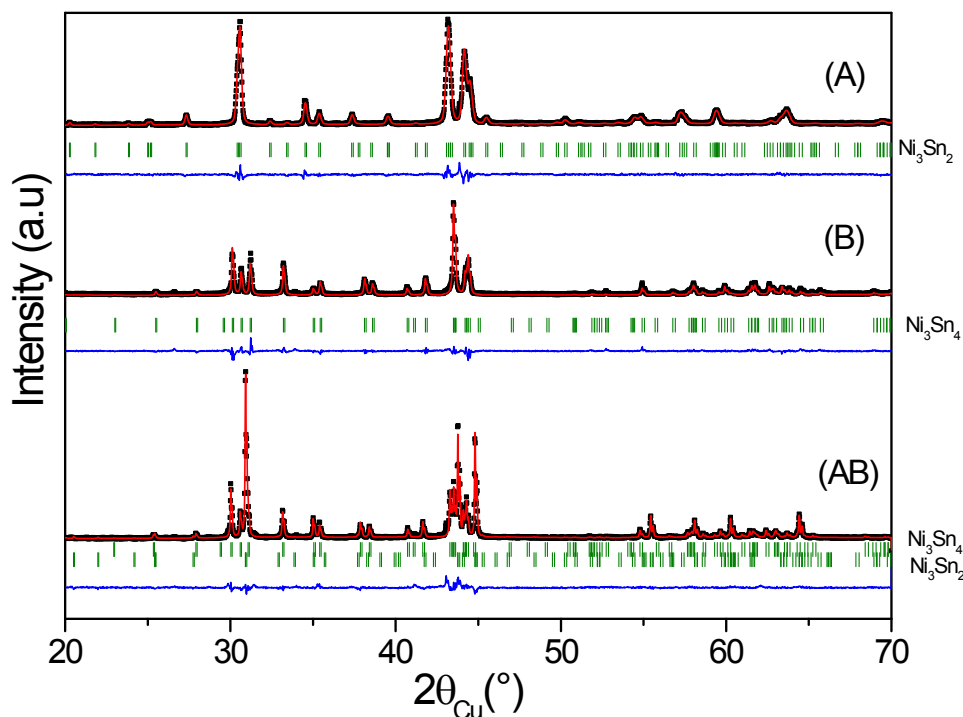
**Fig. S2.** XRD patterns and Rietveld analysis of Ni_3Sn_2 (A), Ni_3Sn_4 (B) and Ni_3Sn_2-Ni_3Sn_4 (AB) samples prepared by powder metallurgy. Observed (dots), calculated (line) and difference (below) curves are shown. The vertical marks show the Bragg positions for all detected phases.

The Mössbauer spectra of samples A (Fig. S3a) and B (Fig. S3b) were fitted with two doublets in agreement with the existence of two Sn crystallographic sites in both Ni_3Sn_2 and Ni_3Sn_4. The values of the Mössbauer parameters are reported in Table S2. The compositions of these two nickel-tin phases were evaluated from the average isomer shift by considering the linear correlation between average isomer shifts (δ_{av}) and atomic percentage of tin (Sn%) for different crystalline phases reported in the literature (Fig. S4)[1]. The Mössbauer spectrum of sample AB was fitted with four doublets corresponding to the two Sn crystallographic sites in Ni_3Sn_2 and Ni_3Sn_4, respectively (Fig. S3c).
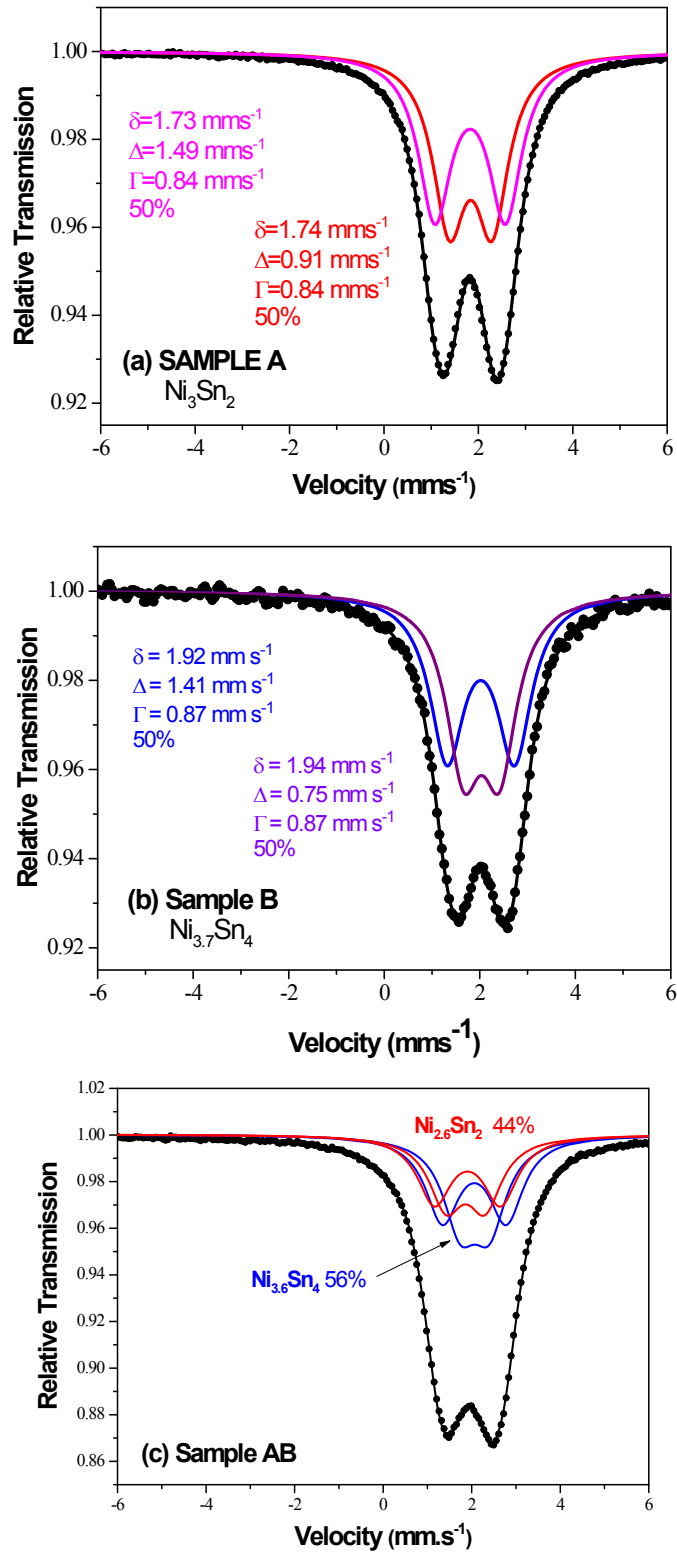
Fig. S3. [119]Sn Mössbauer spectra of samples A (a), B (b) and AB (c) at room temperature. The doublets corresponding to the different Sn crystallographic sites are shown with their relative contributions to the overall spectra.
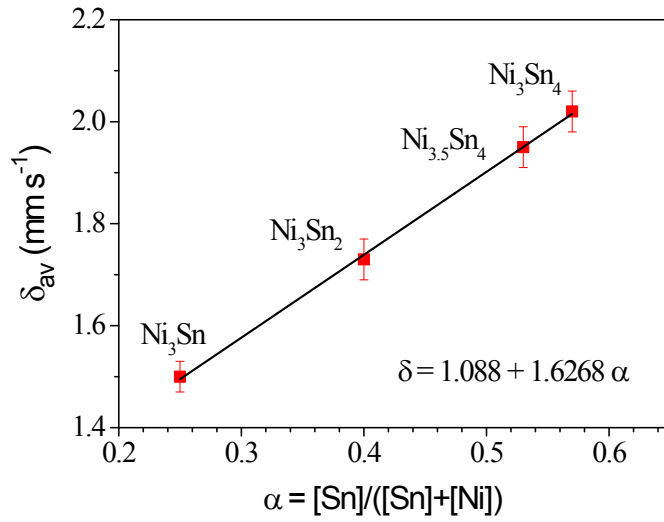
Fig. S4. [119]Sn Average isomer shift of Ni-Sn crystalline phases [1] vs. atomic percentage of Sn. The linear correlation was used to evaluate the composition of the Ni-Sn phases in samples A, B, AB, Si-A, Si-B and Si-AB

Table S2. [119]Sn Mössbauer parameters of samples A, B and AB: isomer shift relative to $BaSnO_3$, δ, quadrupole splitting, Δ, linewidth, Γ, and relative spectral contribution, RSC, and the corresponding assigned phases. The uncertainties on the Mössbauer parameters are lower than 0.05 mm.s^{-1}.

| Sample	Phases	Mössbauer parameters			
		δ, mm.s^{-1}	Δ, mm.s^{-1}	Γ, mm.s^{-1}	RSC, %
A	Ni_3Sn_2	1.73	1.49	0.84*	50*
		1.74	0.91	0.84*	50*
AB	$Ni_{2.7}Sn_2$	1.79	1.49	0.93*	28*
		1.77	0.88	0.93*	28*
	$Ni_{3.6}Sn_4$	1.94	1.44	0.93*	22**
		1.95	0.67	0.93*	22**
B	$Ni_{3.7}Sn_4$	1.92	1.41	0.87*	50*
		1.94	0.75	0.87*	50*

*,** constrained to be equal

Fig. S5 shows TEM analysis for the Si-B composite. The composite morphology is revealed by the bright field TEM image (Fig. S5a). Si domains (bright), with typical size of 150 nm, are embedded in a nanostructured matrix. EFTEM analysis shows that elemental mapping of Ni and Si signal overlaps in agreement with the formation of Ni_3Sn_4 as detected by XRD analysis. The size of Ni_3Sn_4 domains is below 50 nm.
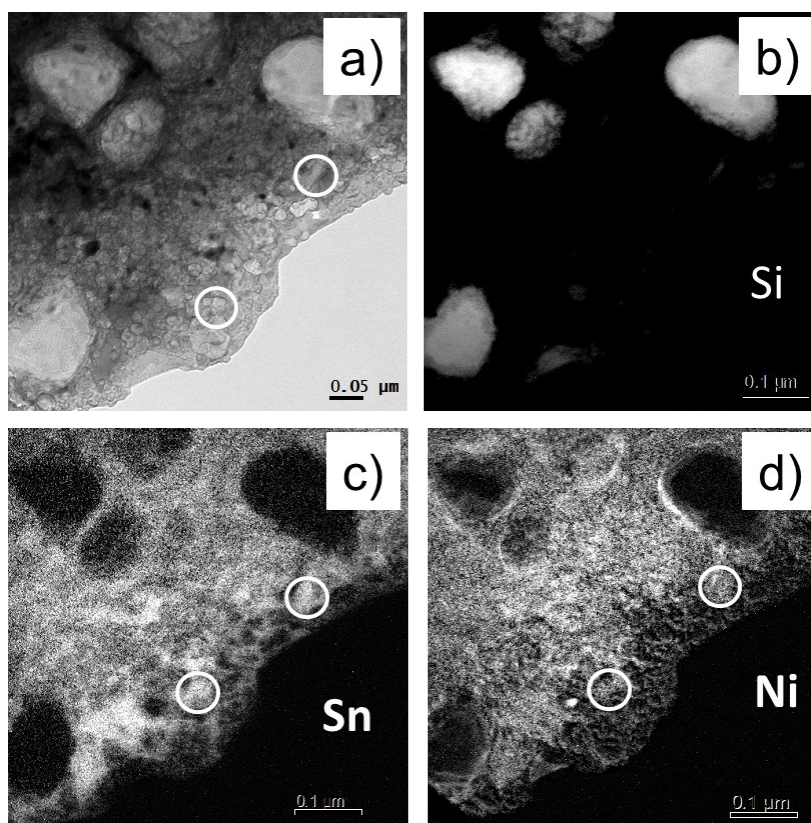

Fig. S5: Morphology of Si-B composite as determined by TEM analysis. a) bright-field TEM image, b) Si- c) Sn- and d) Ni-elemental EFTEM mappings, respectively. Circles are two representative areas showing overlapping of Ni and Sn attributed to the occurrence of Ni_3Sn_4 domains.

Fig. S6 shows the rate capability on charge of the Si-B composite. After slow discharging (i.e. lithiation) of the electrode, the delithiation rate capability is measured for different regimes. High charge capacity is obtained for regime up to 10C.
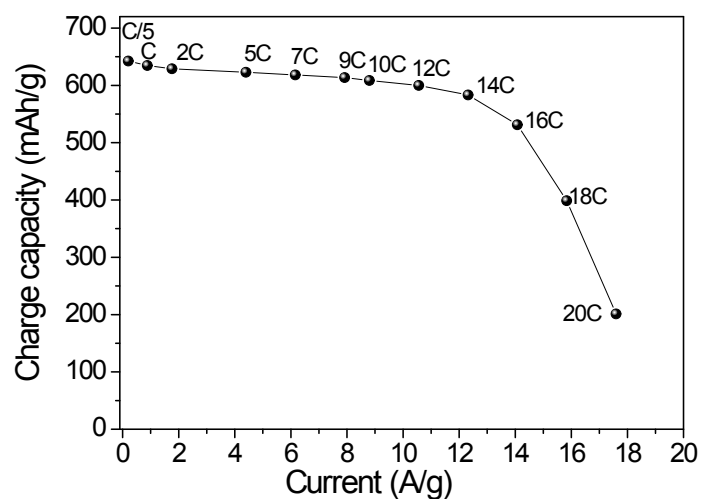
Fig. S6: Charge capacity of the Si-B composite as a function of kinetic regime.

Fig. S7 shows the potential profiles of the representative cycles 2, 80 et 200 (DCP plots shown in Figure 6) for the Si-A, Si-B and Si-AB composites. All potential profiles are smooth, both in charge and discharge, showing a large sloping plateau between ~0.7 V and 70 mV.
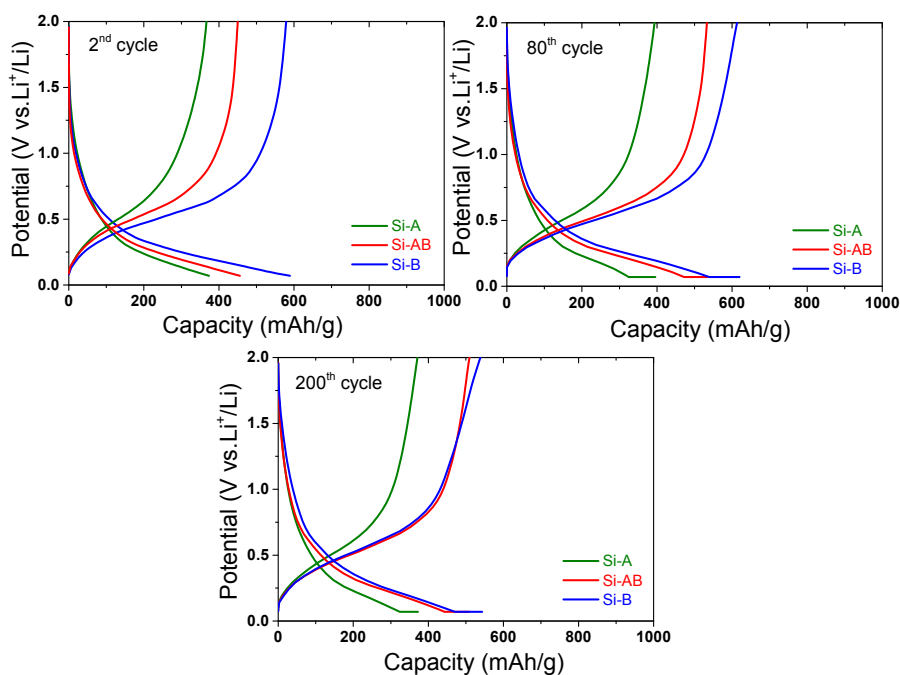
Fig. S7. Discharge/charge profiles of cycles 2, 80 and 200 for the three composite anodes Si-A, Si-B and Si-AB

Table S3 gathers an analysis of the evaluation of Si and Ni_3Sn_4 contributions to the overall capacity of the studied composites. For this evaluation, some hypotheses are necessary. From DCP plots, the deepest lithiation we have detected for Si and Ni_3Sn_4 phases corresponds to the formation of $Li_{3.16}Si$ and Li_7Sn_2 alloys, respectively. Their specific capacities are 3015 and 575 mAh/g, respectively. Considering that all composites contain 19 wt.% of Si, while 0, 32.5 and 65 wt% of Ni_3Sn_4 for Si-A, Si-AB and Si-B, respectively, the overall capacity of the electrodes is 573, 760 and 947 mAh/g, respectively. Contributions from minor Al and C counterparts and inactive Ni_3Sn_2 have not been considered for the sake of simplification. Whatever the composite, the measured reversible capacity at the first cycle (480, 580 and 755 mAh/g) is roughly 80 % of the maximum overall capacity. This suggests that both Si and Ni_3Sn_4 components are lithiated to a similar extent (~ 80%) with respect to their maximum observed loading ($Li_{3.16}Si$ and Li_7Sn_2 alloys, respectively). In the specific case of Si-B composite, maximum contributions of Si and Ni_3Sn_4 are 573 and 374 mAh/g, respectively, being the measured capacity 755 mAh/g, i.e. 80 % of these values.

Table S3. Contribution of Si and Ni_3Sn_4 to the overall specific capacity of the Si/Ni-Sn/Al/C composites assuming the formation of $Li_{3.16}Si$ and Li_7Sn_2 alloys. Nominal phase content, their contribution to the specific capacity, overall capacity ($C_{overall}$), initial capacity (C_{ini}) and their ratio are given.

Sample	Si (wt%)	Ni_3Sn_4 (wt%)	C_{Si} (mAh g^{-1})	$C_{Ni_3Sn_4}$ (mAh g^{-1})	$C_{overall}$ (mAh g^{-1})	C_{ini} (mAh g^{-1})	$C_{ini}/C_{overall}$ (%)
Si-A	19	0	573	0	573	481	84
Si-AB	19	32.5	573	187	760	578	76
Si-B	19	65	573	374	947	756	80

References

1 S. Naille, P. E. Lippens, F. Morato and J. Olivier-Fourcade, *Hyperfine Interact.*, 2006, **167**, 785–790.